

# Improved SnO<sub>2</sub> Electron Transport Layers Solution-Deposited at Near Room Temperature for Rigid or Flexible Perovskite Solar Cells with High Efficiencies

Qingshun Dong, Jiangwei Li, Yantao Shi,\* Min Chen, Luis K. Ono, Ke Zhou, Chunyang Zhang, Yabing Qi, Yuanyuan Zhou, Nitin P. Padture,\* and Liduo Wang\*

Electron transport layer (ETL) is a functional layer of great significance for boosting the power conversion efficiency (PCE) of perovskite solar cells (PSCs). To date, it is still a challenge to simultaneously reduce the surface defects and improve the crystallinity in ETLs during their low-temperature processing. Here, a novel strategy for the mediation of in situ regrowth of SnO<sub>2</sub> nanocrystal ETLs is reported: introduction of controlled trace amounts of surface adsorbed water on the fluorinated tin oxide (FTO) or indium–tin oxide (ITO) surfaces of the substrates using ultraviolet ozone (UVO) pretreatment. The optimum amount of adsorbed water plays a key role in balancing the hydrolysis–condensation reactions during the structural evolution of SnO<sub>2</sub> thin films. This new approach results in a full-coverage SnO<sub>2</sub> ETL with a desirable morphology and crystallinity for superior optical and electrical properties, as compared to the control SnO<sub>2</sub> ETL without the UVO pretreatment. Finally, the rigid and flexible PSC devices based on the new SnO<sub>2</sub> ETLs yield high PCEs of up to 20.5% and 17.5%, respectively.

applications.<sup>[1]</sup> In particular, the record power conversion efficiency (PCE) of perovskite solar cells (PSCs) has seen an extraordinary rise to 24.2% within a relatively short period of time.<sup>[2]</sup> The electron transport layer (ETL) within the multilayer PSCs is of great significance as it performs the key role of extracting and transporting photogenerated electrons. In fact, some of the key advances in PSCs and their stability have been the result of advances in ETL materials and/or structures.<sup>[3]</sup> An ideal ETL should have full coverage, high electronic conductivity (n-type), and few surface trap states, as well as favorable band alignment and intimate contact with the adjacent light-absorber OIHP layer.<sup>[4]</sup> One of the advantages of thin-film PSCs is that they can also be made to be flexible for possible consumer applications. Thus, low-temperature (<150 °C) depo-

sition of ETLs, compatible with plastic substrates, becomes a requirement.<sup>[5]</sup>

While TiO<sub>2</sub> is the most widely used ETL material, recently SnO<sub>2</sub> has proven to be an excellent ETL material, and it is being used more frequently in PSCs with PCEs exceeding 20%.<sup>[6]</sup> In addition to the high chemical stability and low-temperature processability, SnO<sub>2</sub> has higher electronic conductivity, wider bandgap, and excellent optical transparency compared to TiO<sub>2</sub>.<sup>[3c]</sup> Also, SnO<sub>2</sub> ETL has been found to have better band

## 1. Introduction

Organic–inorganic halide perovskites (OIHPs) have recently emerged as a new class of semiconductor material with outstanding characteristics, such as facile solution-processibility, moderate bandgap, strong light-absorption, ultralong carrier-lifetime, etc. These characteristics of thin-film OIHPs make them highly versatile, with great potential for use in solar cells, light-emitting diodes (LEDs), photodetectors, and other

Q. Dong, J. Li, Prof. L. Wang  
Key Lab of Organic Optoelectronics  
Molecular Engineering of Ministry of Education  
Department of Chemistry  
Tsinghua University  
Beijing 100084, China  
E-mail: chldwang@mail.tsinghua.edu.cn

Q. Dong, Prof. Y. Shi, C. Zhang  
State Key Laboratory of Fine Chemicals  
School of Chemistry  
Dalian University of Technology  
Dalian 116024, China  
E-mail: shiyantao@dlut.edu.cn

 The ORCID identification number(s) for the author(s) of this article can be found under <https://doi.org/10.1002/aenm.201900834>.

Q. Dong, M. Chen, Prof. Y. Zhou, Prof. N. P. Padture  
School of Engineering  
Brown University  
Providence, RI 02912, USA  
E-mail: nitin\_padture@brown.edu

Dr. L. K. Ono, Prof. Y. Qi  
Energy Materials and Surface Sciences Unit  
Okinawa Institute of Science and Technology Graduate University  
Okinawa 904-0495, Japan

K. Zhou  
Department of Chemistry  
College of Chemistry and Chemical Engineering  
Xiamen University  
Xiamen 361005, China

DOI: 10.1002/aenm.201900834

alignment, with some of the state-of-the-art OIHP compositions, as compared to  $\text{TiO}_2$  ETL.<sup>[3c,7]</sup> Furthermore, unlike  $\text{TiO}_2$ ,  $\text{SnO}_2$  does not photocatalyze the decomposition of the OIHP layer under solar ultraviolet (UV) irradiation.

Since 2015, the groups of Fang and Yan have jointly conducted extensive research on  $\text{SnO}_2$ -based ETLs, and they have reported some novel strategies for their low-temperature fabrication, nanostructure development, and electrical-properties tuning.<sup>[8]</sup> Very recently, they obtained a high PCE of 20.8% through precise control of the carrier concentration in an ETL based on  $\text{SnO}_2$  quantum dots (QDs).<sup>[6c]</sup> In addition, Hagfeldt and co-workers have fabricated  $\text{SnO}_2$  layers by chemical-bath deposition, and obtained a high PCE of 20.8%.<sup>[6b]</sup> Meanwhile, a certified PCE of 23.3% has been achieved by You and co-workers, whose PSCs with planar architecture use  $\text{SnO}_2$  ETL.<sup>[9]</sup> However, a few key issues regarding  $\text{SnO}_2$  ETL still remain unresolved. For example, enhancing the crystallinity and eliminating surface defects in  $\text{SnO}_2$  ETLs still requires high-temperature heat-treatments (>150 °C). While post-deposition UV-ozone (UVO) is an effective treatment to eliminate surface defects in oxide ETLs at near room temperature, that treatment is ineffective in improving the inherent poor crystallinity of ETLs deposited using low-temperature methods.<sup>[6b,10]</sup> Thus, it is difficult to reduce the surface-defects concentration in  $\text{SnO}_2$  ETL, enhance its crystallinity, and tune the surface roughness simultaneously during low-temperature processing.

Here we elucidate a new approach where UVO pretreatment of fluorinated-tin-oxide (FTO) or indium–tin oxide (ITO) substrate surfaces before the deposition of the  $\text{SnO}_2$  ETLs generates adsorbed water molecules in situ. During subsequent room-temperature sol–gel deposition of  $\text{SnO}_2$  nanocrystallites on the UVO-pretreated substrates, the optimum amount of surface-adsorbed water molecules facilitates optimal hydrolysis–condensation reactions for the regrowth of  $\text{SnO}_2$ . This results in full-coverage  $\text{SnO}_2$  ETL with a desirable morphology and crystallinity for superior optical and electrical properties, as compared to the control  $\text{SnO}_2$  ETL without the UVO pretreatment. Also, the new  $\text{SnO}_2$  ETL has an optimum roughness, which promotes better interfacial electrical coupling with the subsequently solution-deposited OIHP layer. Thus, the resulting improved charge-transfer dynamics yield high PCEs, up to 20.5% (with a steady-state output of 20.1%), in PSCs. Taking advantage of the low-temperature processability, fabrication of flexible PSCs incorporating the new high quality  $\text{SnO}_2$  ETL on plastic substrates with a high PCE of 17.5% is also demonstrated.

## 2. Results and Discussion

UVO is commonly used as a surface-cleaning method that can remove organic residue from substrate surfaces effectively, and increase the surface wettability.<sup>[11]</sup> Thus, it is assumed that water from the atmosphere will adsorb more readily on UVO-pretreated FTO substrates, as illustrated schematically in Figure 1a. As it will be shown later, the amount of surface-adsorbed water depends on the UVO-pretreatment duration, which becomes a critical parameter for controlling the quality of the subsequently deposited  $\text{SnO}_2$  ETL. Figure 1b shows Fourier transform infrared (FTIR) spectra of FTO-coated glass

substrates as a function of UVO-pretreatment duration, where the intensity of the band associated with vibration of hydrogen-containing bonds gradually increases with the UVO-pretreatment duration (0–40 min). At the same time, the band position shifts from  $\approx 3650 \text{ cm}^{-1}$  ( $t = 0 \text{ min}$ ) to  $\approx 3350 \text{ cm}^{-1}$  ( $t = 40 \text{ min}$ ), indicating the formation of intermolecular hydrogen bonds because of more surface-adsorbed water molecules.<sup>[12]</sup> The relative amount of adsorbed water is estimated from Figure 1b, and it is plotted in Figure 1c. (As a reference, the band associated with the underlying glass remains unchanged in Figure 1b.) Thus, the FTIR results indicate that prolonged UVO pretreatment can effectively increase the adsorbed surface-water content on FTO, and hydrogen bonds are inclined to form as more water molecules are adsorbed onto the FTO surface.

The  $\text{SnO}_2$  sol used for the following spin-coating was prepared according to our previous work, which contains  $\text{SnO}_2$  nanocrystallines (<5 nm) dispersed in anhydrous alcohol.<sup>[10b]</sup> The  $\text{SnO}_2$  sol was spin-coated onto the UVO-pretreated FTO substrates for 0–40 min at a fixed ambient humidity ( $\approx 50\% \text{ RH}$ , see the Experimental Section). The  $\text{SnO}_2$  ETLs were subsequently heat-treated at 50 °C for 2 h in air, followed by a 20 min UVO post-treatment. Thus, the only parameter varied here is the UVO-pretreatment duration. Here, our samples are marked using “S-X”, where “X” represents the duration time of UVO-pretreatment (min). The transmittance spectra and photographs in Figure S1 (Supporting Information) show that the two samples of S-10 and S-20 have higher transmittance compared to the bare FTO substrate, consistent with a previous report on the anti-reflection effect of the  $\text{SnO}_2$  films.<sup>[13]</sup> However, the ETLs begin to become foggy and the transmittance decreases as the UVO-pretreatment duration exceeds 20 min, indicating that the UVO-pretreatment has a notable effect on the  $\text{SnO}_2$  ETL optical characteristics.

Scanning electron microscopy (SEM) results are presented in Figure 2a, showing the surface morphology and topography of  $\text{SnO}_2$  ETLs on FTO substrates as a function of UVO-pretreatment duration. Some small cracks and pinholes can be seen in the film without UVO pretreatment (Figure 2a,  $t = 0 \text{ min}$ ). The small amount of organic residue that is omnipresent on the FTO surface before UVO pretreatment can cause poor substrate surface wetting, which can result in the formation of the cracks/pinholes and high roughness during annealing (see Figure S2 in the Supporting Information for variation of film roughness with UVO-pretreatment duration). In contrast, the cracks/pinholes have disappeared in S-10, resulting in a compact, full-coverage thin film with low roughness. Longer UVO pretreatment, for example, in the case of S-20, causes an increase in surface roughness, while further UVO pretreatment ( $t = 40 \text{ min}$ ) results in films with agglomerated  $\text{SnO}_2$  grains and incomplete coverage. The atomic force microscopy (AFM) results (Figure 2b) are consistent with what is observed in the SEM. The conductive AFM (C-AFM) results in Figure 2c clearly show the underlying FTO substrate as high conductivity bright regions in all images except S-20. This confirms full  $\text{SnO}_2$  ETL coverage for UVO-pretreatment duration of 10 and 20 min. Fluorine (F) 1s X-ray photoelectron spectroscopy (XPS) on these  $\text{SnO}_2$  ETLs were also performed, but the results are inconclusive (Figure S3, Supporting Information). This is most likely because the XPS detection depth is <10 nm, whereas C-AFM

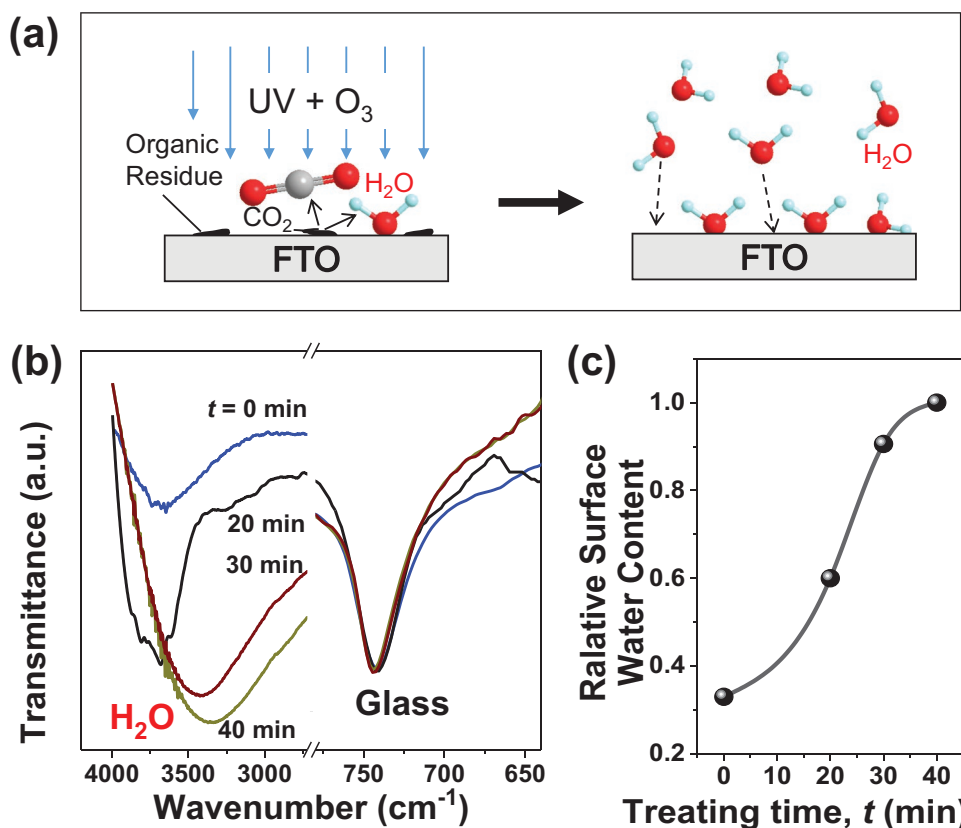


**Figure 1.** a) Schematic illustration of the UVO pretreatment and water adsorption on an FTO substrate. b) FTIR spectra of FTO/glass substrate after UVO pretreatment for different durations. c) Relative surface water content (estimated using the FTIR spectra) as a function of UVO-pretreatment duration.

detection depth is >50 nm. Survey of elements and their related high resolution spectra of Sn 3d and O 1s peaks are also shown in Figure S4 (Supporting Information). The oxygen peak O 1s at

531.2 eV and Sn<sup>4+</sup> peaks at 495.8 eV as well as at 487.4 eV demonstrate that the composition of those films are not changed, and they are all pure SnO<sub>2</sub> films.<sup>[6b]</sup>

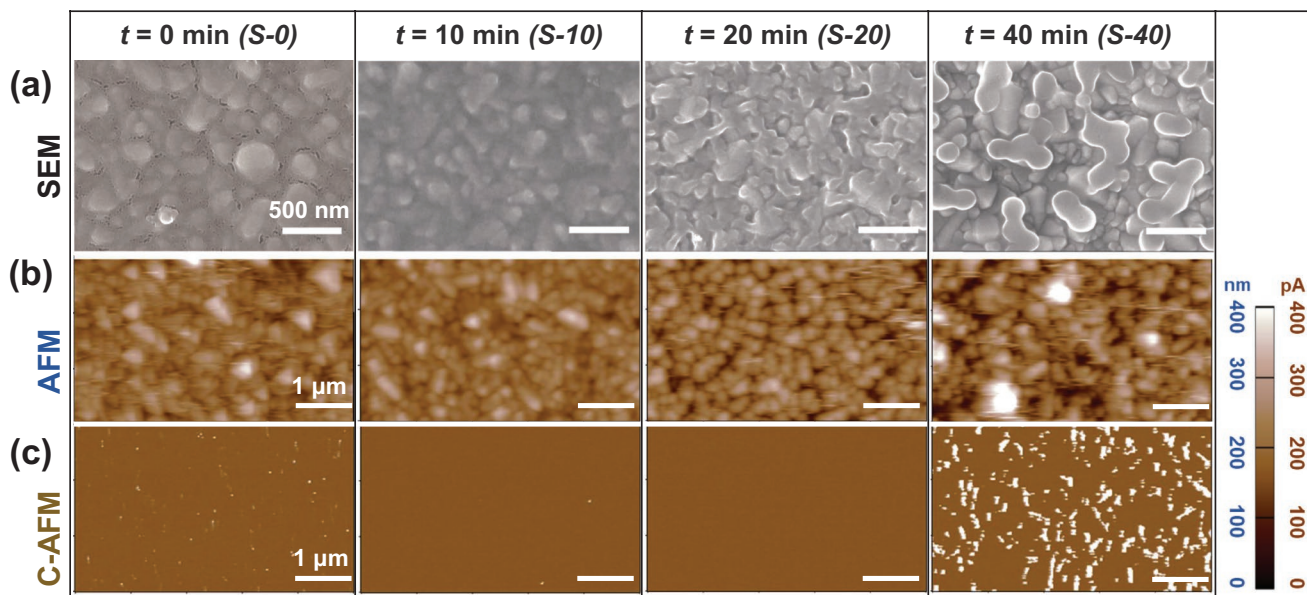


**Figure 2.** Top-surfaces of SnO<sub>2</sub> ETLs on FTO substrates with UVO pretreatment for *t* = 0 min, 10 min, 20 min, and 40 min: a) SEM micrographs, b) AFM images ("nm" scale), and c) corresponding C-AFM mapping ("pA" scale).

The two full-coverage samples of S-10 and S-20 were further characterized, and the Hall-effect mobility of S-20 is found to be  $45.3 \text{ cm}^2 \text{ V}^{-1} \text{ s}^{-1}$ , which is three times higher than that of S-10 ( $15.8 \text{ cm}^2 \text{ V}^{-1} \text{ s}^{-1}$ ). Also, in specimens where the OIHP thin film is deposited on top of the  $\text{SnO}_2$  ETLs (described later), there are gaps at the interface between the OIHP thin film and the  $\text{SnO}_2$  ETL (S-10), as shown in the cross-sectional SEM images in Figure S5 (Supporting Information). In contrast, in the case using S-20 ETL there are no such gaps (Figure S5, Supporting Information) while the interface roughness is relatively high (Figure S2, Supporting Information), which could be advantageous in providing maximum electrical contact between the two layers.<sup>[14]</sup> These results show clearly that there is an optimum UVO-pretreatment duration, which in turn induces the adsorption of an optimum amount of water on the FTO substrate that controls the development of the most desirable  $\text{SnO}_2$  ETL microstructure and morphology. Henceforth, the S-10 ETL is considered as the “reference” film, and the S-20 ETL is considered as the “optimum” film, for a fair comparison as both ETLs are full-coverage.

To demonstrate the key role water concentration plays in the sol-gel synthesis of  $\text{SnO}_2$ , we have performed some model experiments. Here, different amounts of water (10%, 20%, 30%, and 40% in volume) were added to a stable  $\text{SnO}_2$  sol, and the results are summarized in Figure S6 (Supporting Information). Although there is no obvious variation in the appearance of the sol (see photographs in Figure S6a in the Supporting Information) with 10% and 20% water, the dynamic light scattering (DLS) results (Figure S6b, Supporting Information) show that the average colloidal-particles size has increased from  $\approx 3 \text{ nm}$  (0% water) to  $\approx 5 \text{ nm}$  (10% water) to 10–20 nm (20% water). With the addition of more water (30% and 40%), the sol becomes translucent and turbid, with the bimodal particle sizes reach several hundred nanometers and few micrometers. These sols were dried at room temperature, and they were characterized using X-ray diffraction (XRD). The results (Figure S6c, Supporting Information) indicate that the water did not promote the formation of any new phases, but its main effect is on the crystallinity of the  $\text{SnO}_2$  particles. After a certain amount of added water (10–30%) into the sol, the  $\text{SnO}_2$  110 and 101 XRD peaks develop, indicating an increase in the  $\text{SnO}_2$  crystallinity. Dried powders from original  $\text{SnO}_2$  sol and with 20% added water were characterized using transmission electron microscopy (TEM). The results (Figure S7, Supporting Information) show an increase in the  $\text{SnO}_2$  particle size and enhanced crystallinity, which is consistent with the DLS and XRD results. These results confirm that optimum water concentration is needed to obtain desirable crystallinity and size in  $\text{SnO}_2$  particles. However, the ETLs directly prepared by the  $\text{SnO}_2$  sols with different amount water not compact (10% and 20% water samples) or are nonuniform (40% sample) (Figure S8, Supporting Information), resulting in a decrease in the PCE and an increase in the hysteresis in the PSC devices (Figure S9, Supporting Information). This highlights the importance of in situ growth of  $\text{SnO}_2$  nanocrystallines.

It is argued that, in the case of sol-gel deposition of  $\text{SnO}_2$  ETL using spin-coating, a similar optimum amount of water on UVO-pretreated substrates is needed for obtaining high crystallinity and control over the particle size as well as surface

roughness. It is suggested that the hydrolysis of the  $\text{SnO}_2$  sol is inadequate if the amount of adsorbed water on the substrate is deficient ( $t = 0\text{--}10 \text{ min}$ ), resulting in small  $\text{SnO}_2$  particles with poor crystallinity. This is confirmed by TEM characterization of freshly spin-coated  $\text{SnO}_2$  ETL (without the  $50^\circ \text{C}$ -heat-treatment or UVO post-treatment) scraped from the substrate (Figure 3a,b). However, the hydrolysis and condensation reactions occur in a balanced way when there is moderate amount of adsorbed water (in the case of S-20), which can promote oriented attachment of the tiny  $\text{SnO}_2$  nanocrystallites during regrowth resulting in higher crystallinity.<sup>[15]</sup> The TEM image in Figure 3c (S-20) and electron diffraction patterns in Figure S10 (Supporting Information) show evidence for larger  $\text{SnO}_2$  particles with relatively high crystallinity. However, when there is excess adsorbed water (for example, in the case of S-40), the hydrolysis reaction is likely to occur more rapidly, resulting in randomly agglomerated nanoparticles, as evidenced in the TEM image in Figure 3d. Figure 3e is a schematic illustration of the proposed mechanism.

Although methylammonium lead triiodide ( $\text{CH}_3\text{NH}_3\text{PbI}_3$  or  $\text{MAPbI}_3$ ) is the most widely studied OIHP for solar cells, the mixed-composition OIHPs, such as  $\text{Cs}_{0.05}(\text{FA}_{0.85}\text{MA}_{0.15})_{0.95}\text{Pb}(\text{I}_{0.85}\text{Br}_{0.15})_3$ , have been shown to be more suitable light absorbers, and they are also more stable.<sup>[16]</sup> However, the relatively deeper conduction band minimum (CBM) level ( $-4.2 \text{ eV}$ ) of this OIHP (valence band maximum or VBM level  $-5.8 \text{ eV}$ ; bandgap  $1.6 \text{ eV}$ ) makes  $\text{TiO}_2$  ETL unsuitable for PSCs,<sup>[17]</sup> whereas  $\text{SnO}_2$  is ideally suited for efficient electron extraction.<sup>[7a]</sup> Here, we have measured the energy levels of the bands of the reference  $\text{SnO}_2$  ETL (S-10) and the optimum  $\text{SnO}_2$  ETL (S-20) using ultraviolet photoemission spectroscopy (UPS) and UV-vis absorption. As shown in the inset of Figure 4a, the optical bandgap ( $E_g$ ) is estimated to be  $\approx 4.2 \text{ eV}$ . The cutoff energy in Figure 4a is  $\approx 16.8 \text{ eV}$ , and the Fermi level is  $\approx 4.4 \text{ eV}$  below the vacuum level. This results in the VBM level of  $-8.4 \text{ eV}$  (considering photon energy of  $\text{He-I}\alpha$  excitation to be  $21.2 \text{ eV}$ ) and the CBM level of  $-4.2 \text{ eV}$  (considering  $E_g$  of  $\approx 4.2 \text{ eV}$ ). The energy-level diagram is presented in Figure 4b, showing good band alignment for electron and hole transfer, with  $\text{Cs}_{0.05}(\text{FA}_{0.85}\text{MA}_{0.15})_{0.95}\text{Pb}(\text{I}_{0.85}\text{Br}_{0.15})_3$  composition OIHP which is used in the rest of this study.

While the band structures of the reference and the optimum  $\text{SnO}_2$  ETLs are similar, the charge-transfer dynamics and trap-assisted recombination are improved in the optimum  $\text{SnO}_2$  ETL, as shown in Figure 4c,d. Time-resolved photoluminescence (TRPL) results on devices with OIHP layer deposited on top of the optimum  $\text{SnO}_2$  ETL in Figure 4c reveal rapid decay, with carrier (electrons) lifetimes of  $\tau_1 = 3.0 \text{ ns}$  and  $\tau_2 = 28.0 \text{ ns}$  (two-parameter curve fitting). In comparison, the reference  $\text{SnO}_2$  ETL carrier lifetimes are somewhat longer:  $\tau_1 = 3.4 \text{ ns}$  and  $\tau_2 = 31.9 \text{ ns}$ , suggesting less efficient electrons quenching by that ETL. Full PSC devices with n-i-p architecture,  $\text{FTO}/\text{SnO}_2/\text{Cs}_{0.05}(\text{FA}_{0.85}\text{MA}_{0.15})_{0.95}\text{Pb}(\text{I}_{0.85}\text{Br}_{0.15})_3/\text{Spiro-OMeTAD}/\text{Au}$ , were also fabricated. Figure 4d is a semilogarithmic plot of the measured  $V_{\text{OC}}$  of the PSCs as a function of incident light intensity, showing near-ideal  $kT/q$  slope of 1.1 indicating reduced trap-assisted recombination in the PSC with the optimum  $\text{SnO}_2$  ETL (slope is 1.37 for PSC with the reference  $\text{SnO}_2$  ETL). The improved properties of the optimum  $\text{SnO}_2$  ETL are attributed to its improved crystallinity and larger grain size.

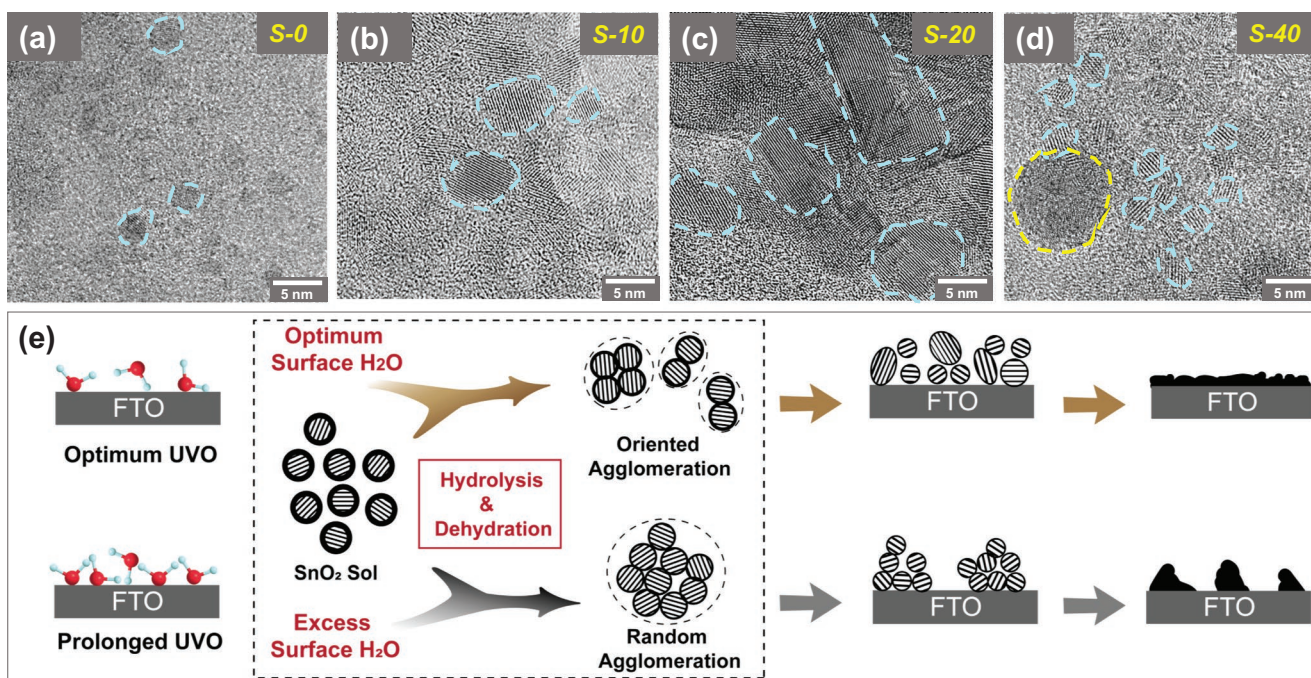


**Figure 3.** TEM images of freshly spin-coated SnO<sub>2</sub> ETL scraped off from FTO substrates that were UVO-pretreated for  $t =$ : a) 0 min, b) 10 min, c) 20 min, and d) 40 min. The turquoise and yellow dashed circles denote single-nanocrystals and clusters, respectively. e) Schematic illustration of the proposed mechanisms for the structural evolution of SnO<sub>2</sub> thin films on FTO substrates with optimum and excess adsorbed water.

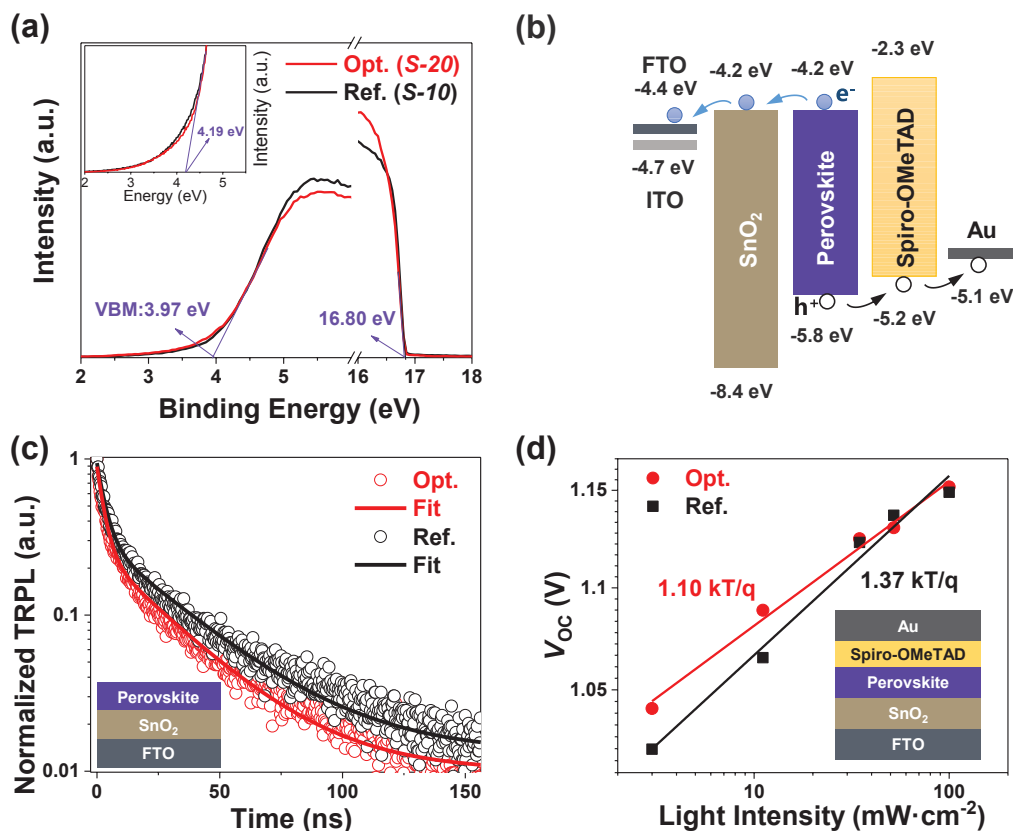


**Figure 4.** a) UPS spectra showing the Fermi edge (left) and cut-off energy (right) of reference (S-10) and optimum (S-20) SnO<sub>2</sub> ETLs. Inset: Corresponding UV-vis spectra. b) Energy levels diagram for the n-i-p PSC device structure. c) TRPL data for OIHP on reference and optimum SnO<sub>2</sub> ETLs (inset: device structure schematic). d) V<sub>oc</sub> as a function of incident light intensity for PSCs with reference and optimum SnO<sub>2</sub> ETLs (inset: device structure schematic).

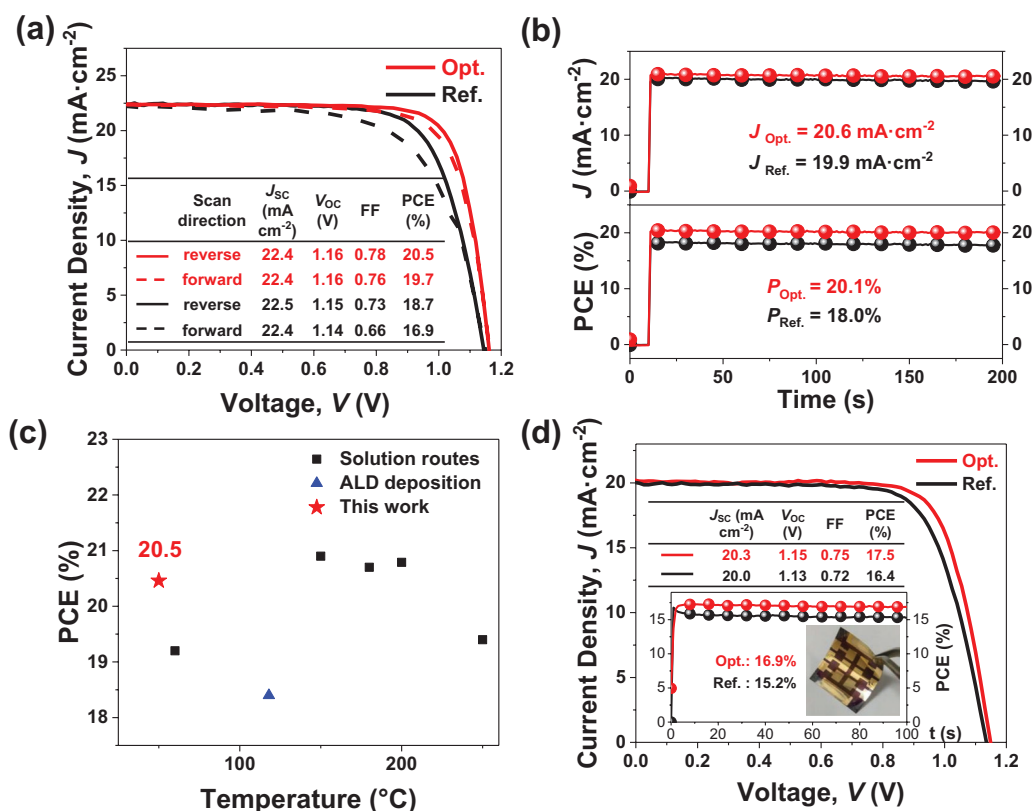


**Figure 5.** a)  $J$ - $V$  curves and PV parameters (inset) and b) steady-state output of photocurrent and PCE of the champion cells using reference (Ref.) and optimum (Opt.) ETLs. c) Highest performing PSCs on SnO<sub>2</sub> ETLs prepared at different temperatures. d) Performance of champion flexible devices on the reference and optimum SnO<sub>2</sub> ETLs.

The PV performance of PSCs with SnO<sub>2</sub> ETLs on FTO substrates UVO-pretreated for  $t = 0, 10, 20, 30,$  or  $40$  min were measured. The PV-performance data and statistics are presented in Figure S11 (Supporting Information), and they are summarized in Table S1 (Supporting Information). These results indicate clearly that optimum UVO-pretreatment, for optimum amount of adsorbed water on FTO substrates, gives the best SnO<sub>2</sub> ETL for maximum PV performance. **Figure 5a** presents current density–voltage ( $J$ - $V$ ) curves and the extracted PV-performance data (inset table) for “champion” PSCs with reference and optimum SnO<sub>2</sub> ETLs. Although both PSCs show hysteresis, it is much more pronounced in the reference PSC. Both PSCs have similar short-circuit current density ( $J_{sc}$ ) values (22.4–22.5 mA cm<sup>-1</sup>, reverse scan), but the open-circuit voltage ( $V_{oc}$ ) of the PSC with optimum ETL (1.16 V, reverse scan) is somewhat higher, and the fill factor (FF) is significantly improved (0.78, reverse scan). The highest PCE of the PSC with optimum ETL is 20.5% (reverse scan) compared to 18.7% for the PSC with reference ETL. Maximum power-point  $J$  and PCE for PSCs with reference and optimum ETL are plotted in Figure 5b, showing steady PV performance. The  $J$ - $V$  responses of other PSCs with reference and optimum SnO<sub>2</sub> ETLs are presented in Figure S12a (Supporting Information), which also show a similar trend. The external quantum efficiency (EQE) and the integrated  $J_{sc}$  data are presented in Figure S12b (Supporting Information), where the  $J_{sc}$  measured from the  $J$ - $V$  curve (22.4 mA cm<sup>-2</sup>, reverse scan) is consistent with that

from EQE spectrum (21.8 mA cm<sup>-2</sup>) for the optimum PSC. The average series ( $R_s$ ) and shunt ( $R_{sh}$ ) resistance values of the PSC with reference ETL were measured to be 7.1 and 5573  $\Omega$  cm<sup>2</sup>, respectively, whereas they are 5.5 and 6182  $\Omega$  cm<sup>2</sup>, respectively, for the PSC with optimum ETL. The simultaneous decrease in  $R_s$  and an increase in  $R_{sh}$  suggest improved charge-transfer dynamics in the PSC with optimum SnO<sub>2</sub> ETL, which appears to be responsible for the overall improved PV performance.

It has been shown that trapped charge can induce irreversible degradation of OIHPs,<sup>[3a,18]</sup> and both the presence of trap states at the ETL/OIHP interface and the low charge mobility of the ETL could impede the electron transfer. Therefore, it is reasonable to speculate that improved charge transport and reduced trap state density between the optimum SnO<sub>2</sub> ETL and the OIHP layer can result in a more stable device. To verify this hypothesis, unencapsulated PSCs with reference and optimum SnO<sub>2</sub> ETLs were stored at room temperature in a desiccator (humidity < 20%) in dark, and their PCEs were measured in ambient atmosphere about every 5 days. As shown in Figure S13 (Supporting Information), after 50 days of storage, PSC with optimum SnO<sub>2</sub> ETLs shows almost no degradation, whereas the PCE of the PSC with reference SnO<sub>2</sub> ETLs has degraded to 90% of the original value.

We also put this work in the context of other studies; Figure 5c plots maximum PCE achieved against the highest temperature needed for the deposition of SnO<sub>2</sub> ETLs in PSCs.<sup>[6b]-[d,7a,19]</sup> It can be clearly seen that the temperature for

tuning the ETL crystallinity and microstructure in this work is the lowest among these relevant studies. Thus, taking advantage of the low-temperature (50 °C) processing of high quality SnO<sub>2</sub> ETLs, flexible PSCs on plastic substrates (polyethylene naphthalate or PEN with ITO) were fabricated with reference or optimum SnO<sub>2</sub> ETL (same PSC architecture as above). Figure 5d presents the *J*-*V* curves and PV-performance data for the “champion” PSCs, showing 17.5% maximum PCE (16.9% steady-state PCE) using optimum SnO<sub>2</sub> ETL, compared with 16.9% maximum PCE (15.4% steady-state PCE) using reference SnO<sub>2</sub> ETL. The >17% PCE is comparable to PCEs of state-of-the-art flexible PSCs.<sup>[20]</sup>

### 3. Conclusions

In conclusion, we have demonstrated a new strategy for simultaneously tuning the crystallinity, density of trap states, and surface roughness in SnO<sub>2</sub> ETL used in PSCs at near room temperature. The key to this new method is the regrowth of SnO<sub>2</sub> nanocrystallines triggered by the water absorbed on the FTO or ITO surfaces introduced by UVO pretreatment. It was found that the amount of water is a critical factor for obtaining high quality SnO<sub>2</sub> ETLs through balanced hydrolysis–condensation reactions. As compared to control SnO<sub>2</sub> ETL, our new SnO<sub>2</sub> ETL has improved optical and electrical properties. Also, a relatively rough surface ensured that the new SnO<sub>2</sub> ETL bonds tightly with the OIHP layer, providing good interfacial electrical coupling. The structural advantages of the new ETL results in an improvement in charge transfer dynamics, by which the energy loss within PSCs is further minimized, and a notable enhancement in PCE is achieved as a result. Finally, PSC devices based on our new SnO<sub>2</sub> ETL show high PCEs up to 20.5%, with a steady-state output of 20.1%. In the case of flexible PSC, a high PCE of 17.5% is obtained using the new SnO<sub>2</sub> ETL.

### 4. Experimental Section

**Materials and Reagents:** All the chemicals were used as received, including PbI<sub>2</sub> and PbBr<sub>2</sub> (>99%, TCI), CH<sub>3</sub>NH<sub>3</sub>Br (MABr, Xi’an Polymer Light Technology Corp), NH<sub>4</sub>CH<sub>3</sub>NH<sub>2</sub>I (FAI, Xi’an Polymer Light Technology Corp), CsI (99.999%, Alfa Aesar), SnCl<sub>2</sub>·2H<sub>2</sub>O (98–103%, Alfa Aesar), Spiro-OMeTAD (99.7%, Lumtec Co., Taiwan), ethanol (99.8%, Sinopharm Chemical Reagent Co., Ltd), FK209 (98%, HeptaChroma), 4-*tert*-butylpyridine (TBP, 96%), bis(trifluoromethane) sulfonimide lithium salt (99.95%), and solvents acetonitrile (99.9%), dimethylformamide (DMF, 99.8%), dimethylsulfoxide (DMSO, 99.9%), and chlorobenzene (CB, 99.8%) were all purchased from Sigma Aldrich. Fluorinated tin oxide (FTO)-coated glass substrates (7 Ω sq<sup>-1</sup>) and ITO-coated polyethylene naphthalate (PEN) substrates (15 Ω sq<sup>-1</sup>) were purchased from Yingkou OPVtech New Energy Co. Ltd.

**SnO<sub>2</sub> Sol Preparation:** SnCl<sub>2</sub>·2H<sub>2</sub>O sol was prepared by dissolving SnCl<sub>2</sub>·2H<sub>2</sub>O in anhydrous ethanol (0.1 M) in an open reflux apparatus and stirred at 80 °C for 3 h. After standing at 40 °C for 3 h, the sol was aged for 24 h at room temperature.

**SnO<sub>2</sub> ETL Preparation:** FTO/glass or the ITO/PEN substrates were etched with zinc powder and 4 M HCl to obtain the electrode pattern, and then washed with cleaning fluid, deionized water, ethanol (99.7%, Sinopharm), acetone (99.5%, Beijing Shiji), and isopropanol (99.7%, Sinopharm) sequentially. The substrate surface absorbed

water was controlled by the ambient humidity and ultraviolet-ozone (UVO) pretreatment duration. The ambient condition has significant influence on the performance and reproducibility of the ETLs: when the ambient humidity is less than 40% RH, even if a long duration (>1 h) UVO pretreatment, the surface moisture is not enough to cause the change of film structure; when the ambient humidity is larger than 60% RH, it is too easy to cause excessive moisture on the surface, making it difficult to control the film quality; the optimum ambient humidity is ≈50% RH, at this condition the surface water could be controlled by the UVO pretreatment duration as shown in the manuscript. So, for better repeatability, FTO/glass and ITO/PEN substrates were then pretreated with UVO for different duration (0–40 min) under ≈50% RH ambient conditions. Subsequently, SnO<sub>2</sub> sol (no water added) was spin-coated on the substrates at 2000 rpm for 30 s, and then heated at 50 °C for 2 h to remove the solvent. All ETLs were then UVO-post-treated for 20 min. The typical thickness of the ETL is 70–100 nm. Finally, the ETL substrates were transferred to the dry air glove box (H<sub>2</sub>O < 0.01 ppm) for organic–inorganic halide perovskite (OIHP) deposition below.

**OIHP Thin Film Preparation:** OIHP of composition Cs<sub>0.05</sub>(FA<sub>0.85</sub>MA<sub>0.15</sub>)<sub>0.95</sub>Pb(I<sub>0.85</sub>Br<sub>0.15</sub>)<sub>3</sub> was prepared using a procedure described in a previous report.<sup>[6b]</sup> First, anhydrous mixture of DMF and DMSO (4:1 by volume) containing FAI (1 M), PbI<sub>2</sub> (1.1 M), MABr (0.2 M), and PbBr<sub>2</sub> (0.22 M) was prepared by stirring at 60 °C for 0.5 h. Subsequently, 50 μL 1.5 M solution of CsI in DMSO was added to the above solution. To prepare the perovskite films, 50 μL solution was spread on the SnO<sub>2</sub>-ETL/FTO/glass or the SnO<sub>2</sub>-ETL/ITO/PEN substrates, followed by a two-stage spin-coating processes (1000 rpm for 10 s and 6000 rpm for 20 s). During the second spin coating stage, 100 μL of chlorobenzene were dripped on the spinning substrate 5 s prior the end of spin-coating. Finally, the substrates were annealed at 100 °C for 50 min. This resulted in an OIHP thin film of 600 nm thickness.

**Hole Transport Layer (HTL) and Au Electrode Preparation:** Precursor solution of HTL was prepared by dissolving 72.3 mg spiro-MeOTAD, 28.8 μL 4-*tert*-butylpyridine, 17.5 μL lithium bis (trifluoromethylsulfonyl) imide acetonitrile solution (520 mg mL<sup>-1</sup>) into 1 mL chlorobenzene. Subsequently, HTL was deposited on top of the OIHP layer by spin coating at 3000 rpm for 30 s. Typical thickness of the HTL is ≈250 nm. Finally, a 60 nm Au electrode was thermally evaporated on top of the HTL. The active area of the device was 0.16 cm<sup>2</sup>, as defined by a nonreflective mask.

**Characterizations:** To demonstrate the key role water plays in the regrowth of SnO<sub>2</sub> nanocrystalline in the sol, different amounts of water (10%, 20%, 30%, and 40% in volume) were added into above stable SnO<sub>2</sub> sol. The size distributions of SnO<sub>2</sub> particles were measured using SZ-100Z analyzer (Horiba). Transmission electron microscopy (TEM) was performed on 2100F (JEOL) instrument using an acceleration voltage of 200 KV. To observe the SnO<sub>2</sub> nanoparticles, 20-fold diluted original SnO<sub>2</sub> sol (5 μL) was dripped onto holey-carbon TEM grids, and the dried in air at room temperature for 6 h. X-ray diffraction (XRD) of the SnO<sub>2</sub> powders and thin films (on quartz substrate) was performed using a high-resolution diffractometer (D8 Advance, Bruker; Germany) with Cu Kα radiation. To avoid the temperature’s affection on the crystallinity of SnO<sub>2</sub> nanocrystallines, these sols with different amount of water were dried at room temperature for 48 h to get the SnO<sub>2</sub> powders.

For the SnO<sub>2</sub> ETLs, the as-spin-coated films (without heat-treatment or UVO post-treatment) were scraped off and dispersed in anhydrous ethanol. About 5 μL of this suspension was dripped onto holey-carbon TEM grids and dried at room temperature for 6 h. SEM images were acquired using JSM-7401F (JEOL) and Merlin (Zeiss) field-emission instruments.

Atomic force microscope (AFM) and conductive AFM (C-AFM) images of FTO and SnO<sub>2</sub> ETL surfaces were obtained using MFP-3D (Asylum Research) instrument. A conducting Pt-coated Si tip (Econo-SCM-PIC, Asylum Research) was used. All the SnO<sub>2</sub> thin films on FTO were connected to the substrate with Ag paste. No bias voltage was applied to obtain the C-AFM images to exclude any possible tunneling effects.

Transmittance spectra were recorded using U-3900 spectrophotometer (Hitachi). Photoluminescence (PL) lifetime was measured by FLIM with a FV1200 laser scanning confocal microscope (Olympus). A 488 nm

pulsed diode laser was used for excitation. The emission was filtered through a 50/50 dichroic beam splitter and a 700–800 nm long pass filter. FTIR of the UVO-pretreated FTO substrates were obtained in attenuated total reflection (ATR) mode using V70 spectrometer (Bruker). XPS was performed using Kratos Analytical spectrometer (AXIS ULTRA HAS, monochromated Al  $K\alpha = 1486.6$  eV) and all XPS spectra were shifted to account for sample charging using inorganic carbon at 284.80 eV as a reference. UPS was performed using Kratos Analytical spectrometer (AXIS ULTRA DLD), and monochromatized He  $I\alpha$  radiation at 21.2 eV was used.

Hall-effect measurements on the SnO<sub>2</sub> ETLs were performed on a device with four-Ga electrode system using 2400 SourceMeter (Keithley).

The current density–voltage ( $J$ – $V$ ) characteristics of PSCs were measured 2400 SourceMeter (Keithley) at the scan speed of 100 mV s<sup>-1</sup> under AM 1.5G one-sun illumination (100 mW cm<sup>-2</sup>) generated by an Solar 3A (Oriel) solar simulator. The intensity was calibrated using a VLSI standard incorporated PN 91150 V Si reference cell. The PSCs were masked using a black metal mask with a hole area of 0.096 cm<sup>2</sup>. Steady-state output of current density and PCE were measured using 2400 SourceMeter (Keithley) under a certain bias. The EQE spectra were obtained using IQE 200B quantum efficiency measurement system (Oriel). For long-term stability testing, the devices were stored in the dark in a dry box, and the  $J$ – $V$  test was measured regularly.

## Supporting Information

Supporting Information is available from the Wiley Online Library or from the author.

## Acknowledgements

This research was funded primarily by the National Natural Science Foundation of China (Grant Nos. 91433205, 51773025, and 51872036), Tsinghua University Initiative Scientific Research Program and the Fundamental Research Funds for the Central Universities (Grant No. DUT18ZD208). The work at Brown University was funded by the US National Science Foundation (OIA-1538893). L.K.O. and Y.B.Q. acknowledge the funding support from the Energy Materials and Surface Sciences Unit of the Okinawa Institute of Science and Technology Graduate University, the OIST Proof of Concept (POC) Program, the OIST R&D Cluster Research Program, and JSPS KAKENHI Grant Number JP18K05266. The authors are grateful to M. Shen for his assistance with the TEM characterization.

## Conflict of Interest

The authors declare no conflict of interest.

## Keywords

morphological control, nanocrystal regrowth, perovskite solar cells, room temperature, tin dioxide

Received: March 13, 2019

Revised: April 26, 2019

Published online: May 28, 2019

[1] a) M. Chen, M.-G. Ju, M. Hu, Z. Dai, Y. Hu, Y. Rong, H. Han, X. C. Zeng, Y. Zhou, N. P. Padture, *ACS Energy Lett.* **2019**, *4*, 276;

- b) M. V. Kovalenko, L. Protesescu, M. I. Bodnarchuk, *Science* **2017**, *358*, 745; c) Y. Liu, Y. Zhang, Z. Yang, H. Ye, J. Feng, Z. Xu, X. Zhang, R. Munir, J. Liu, P. Zuo, Q. Li, M. Hu, L. Meng, K. Wang, D.-M. Smilgies, G. Zhao, H. Xu, Z. Yang, A. Amassian, J. Li, K. Zhao, S. Liu, *Nat. Commun.* **2018**, *9*, 5302; d) M. Chen, M.-G. Ju, A. D. Carl, Y. Zong, R. L. Grimm, J. Gu, X. C. Zeng, Y. Zhou, N. P. Padture, *Joule* **2018**, *2*, 558; e) H. Guo, J. Zhao, Q. Dong, L. Wang, X. Ren, S. Liu, C. Zhang, G. Dong, *Nano Energy* **2019**, *56*, 391.
- [2] a) M. M. Lee, J. Teuscher, T. Miyasaka, T. N. Murakami, H. J. Snaith, *Science* **2012**, *338*, 643; b) H.-S. Kim, C.-R. Lee, J.-H. Im, K.-B. Lee, T. Moehl, A. Marchioro, S.-J. Moon, R. Humphry-Baker, J.-H. Yum, J. E. Moser, *Sci. Rep.* **2012**, *2*, 591; c) J.-W. Lee, Z. Dai, C. Lee, H. M. Lee, T.-H. Han, N. De Marco, O. Lin, C. S. Choi, B. Dunn, J. Koh, D. Di Carlo, J. H. Ko, H. D. Maynard, Y. Yang, *J. Am. Chem. Soc.* **2018**, *140*, 6317; d) N. J. Jeon, H. Na, E. H. Jung, T.-Y. Yang, Y. G. Lee, G. Kim, H.-W. Shin, S. Il Seok, J. Lee, J. Seo, *Nat. Energy* **2018**, *3*, 682; e) NREL best research-cell efficiency chart, <https://www.nrel.gov/pv/cell-efficiency.html> (accessed: April 2019).
- [3] a) H. Tan, A. Jain, O. Voznyy, X. Lan, F. P. Garcia de Arquer, J. Z. Fan, R. Quintero-Bermudez, M. Yuan, B. Zhang, Y. Zhao, F. Fan, P. Li, L. N. Quan, Y. Zhao, Z.-H. Lu, Z. Yang, S. Hoogland, E. H. Sargent, *Science* **2017**, *355*, 722; b) S. S. Shin, E. J. Yeom, W. S. Yang, S. Hur, M. G. Kim, J. Im, J. Seo, J. H. Noh, S. I. Seok, *Science* **2017**, *356*, 167; c) Q. Jiang, L. Zhang, H. Wang, X. Yang, J. Meng, H. Liu, Z. Yin, J. Wu, X. Zhang, J. You, *Nat. Energy* **2017**, *2*, 16177; d) B. Roose, Q. Wang, A. Abate, *Adv. Energy Mater.* **2019**, *9*, 1803140; e) M. M. Tavakoli, P. Yadav, R. Tavakoli, J. Kong, *Adv. Energy Mater.* **2018**, *8*, 1800794.
- [4] L. Xiong, Y. Guo, J. Wen, H. Liu, G. Yang, P. Qin, G. Fang, *Adv. Funct. Mater.* **2018**, *28*, 1802757.
- [5] Y. Wang, S. Bai, L. Cheng, N. Wang, J. Wang, F. Gao, W. Huang, *Adv. Mater.* **2016**, *28*, 4532.
- [6] a) Q. Dong, Y. Shi, K. Wang, Y. Li, S. Wang, H. Zhang, Y. Xing, Y. Du, X. Bai, T. Ma, *J. Phys. Chem. C* **2015**, *119*, 10212; b) E. H. Anaraki, A. Kermanpur, L. Steier, K. Domanski, T. Matsui, W. Tress, M. Saliba, A. Abate, M. Grätzel, A. Hagfeldt, J.-P. Correa-Baena, *Energy Environ. Sci.* **2016**, *9*, 3128; c) G. Yang, C. Chen, F. Yao, Z. Chen, Q. Zhang, X. Zheng, J. Ma, H. Lei, P. Qin, L. Xiong, W. Ke, G. Li, Y. Yan, G. Fang, *Adv. Mater.* **2018**, *30*, 1706023; d) Q. Jiang, Z. Chu, P. Wang, X. Yang, H. Liu, Y. Wang, Z. Yin, J. Wu, X. Zhang, J. You, *Adv. Mater.* **2017**, *29*, 1703852.
- [7] a) J. P. Correa Baena, L. Steier, W. Tress, M. Saliba, S. Neutzner, T. Matsui, F. Giordano, T. J. Jacobsson, A. R. Srimath Kandada, S. M. Zakeeruddin, A. Petrozza, A. Abate, M. K. Nazeeruddin, M. Grätzel, A. Hagfeldt, *Energy Environ. Sci.* **2015**, *8*, 2928; b) Q. Dong, Y. Shi, C. Zhang, Y. Wu, L. Wang, *Nano Energy* **2017**, *40*, 336.
- [8] W. Ke, G. Fang, Q. Liu, L. Xiong, P. Qin, H. Tao, J. Wang, H. Lei, B. Li, J. Wan, G. Yang, Y. Yan, *J. Am. Chem. Soc.* **2015**, *137*, 6730.
- [9] Q. Jiang, Y. Zhao, X. Zhang, X. Yang, Y. Chen, Z. Chu, Q. Ye, X. Li, Z. Yin, J. You, *Nat. Photonics* **2019**, <https://doi.org/10.1038/s41566-019-0398-2>.
- [10] a) M. Park, J.-Y. Kim, H. J. Son, C.-H. Lee, S. S. Jang, M. J. Ko, *Nano Energy* **2016**, *26*, 208; b) Q. S. Dong, Y. T. Shi, C. Y. Zhang, Y. K. Wu, L. D. Wang, *Nano Energy* **2017**, *40*, 336.
- [11] W. Ke, G. Fang, J. Wan, H. Tao, Q. Liu, L. Xiong, P. Qin, J. Wang, H. Lei, G. Yang, M. Qin, X. Zhao, Y. Yan, *Nat. Commun.* **2015**, *6*, 6700.
- [12] T. L. Tso, E. K. Lee, *J. Phys. Chem.* **1985**, *89*, 1612.
- [13] L. Xiong, M. Qin, G. Yang, Y. Guo, H. Lei, Q. Liu, W. Ke, H. Tao, P. Qin, S. Li, H. Yu, G. Fang, *J. Mater. Chem. A* **2016**, *4*, 8374.

- [14] D. Liu, S. Li, P. Zhang, Y. Wang, R. Zhang, H. Sarvari, F. Wang, J. Wu, Z. Wang, Z. D. Chen, *Nano Energy* **2017**, *31*, 462.
- [15] C. J. Dalmaschio, C. Ribeiro, E. R. Leite, *Nanoscale* **2010**, *2*, 2336.
- [16] M. Saliba, T. Matsui, J.-Y. Seo, K. Domanski, J.-P. Correa-Baena, M. K. Nazeeruddin, S. M. Zakeeruddin, W. Tress, A. Abate, A. Hagfeldt, *Energy Environ. Sci.* **2016**, *9*, 1989.
- [17] C. Zhang, Y. Shi, S. Wang, Q. Dong, Y. Feng, L. Wang, K. Wang, Y. Shao, Y. Liu, S. Wang, *J. Mater. Chem. A* **2018**, *6*, 17882.
- [18] N. Ahn, K. Kwak, M. S. Jang, H. Yoon, B. Y. Lee, J.-K. Lee, P. V. Pikhitsa, J. Byun, M. Choi, *Nat. Commun.* **2016**, *7*, 13422.
- [19] a) D. Yang, R. Yang, K. Wang, C. Wu, X. Zhu, J. Feng, X. Ren, G. Fang, S. Priya, S. F. Liu, *Nat. Commun.* **2018**, *9*, 3239; b) K.-H. Jung, J.-Y. Seo, S. Lee, H. Shin, N.-G. Park, *J. Mater. Chem. A* **2017**, *5*, 24790.
- [20] D. Yang, R. Yang, S. Priya, S. F. Liu, *Angew. Chem., Int. Ed.* **2019**, *58*, 4466.